A Four-Plate Compact Capacitive Coupler Design and *LCL*-Compensated Topology for Capacitive Power Transfer in Electric Vehicle Charging Application

Hua Zhang, *Student Member, IEEE*, Fei Lu, *Student Member, IEEE*, Heath Hofmann, *Senior Member, IEEE*, Weiguo Liu, *Senior Member, IEEE*, and Chunting Chris Mi, *Fellow, IEEE*

***Abstract*—This paper proposes a four-plate compact capacitive coupler and its circuit model for large air-gap distance capacitive power transfer (CPT). The four plates are arranged vertically, instead of horizontally, to save space in the electric vehicle charging application. The two plates that are on the same side are placed close to each other to maintain a large coupling capacitance, and they are of different sizes to maintain the coupling between the primary and secondary sides. The circuit model of the coupler is presented, considering all six coupling capacitors. The *LCL* compensation topology is used to resonate with the coupler and provide high voltage on the plates to transfer high power. The circuit model of the coupler is simplified to design the parameters of the compensation circuit. Finite-element analysis is employed to simulate the coupling capacitance and design the dimensions of the coupler. The circuit performance is simulated in LTspice to design the specific parameter values. A prototype of the CPT system was designed and constructed with the proposed vertical plate structure. The prototype achieved an efficiency of 85.87% at 1.88-kW output power with a 150-mm air-gap distance.**

***Index Terms*—Capacitive power transfer, electric coupling, electric field, electric vehicle (EV) charging, equivalent capacitor model, four-plate structure, high-frequency wireless power transfer, *LCL* compensation topology.**

Manuscript received August 16, 2015; revised November 20, 2015; accepted January 15, 2016. Date of publication January 22, 2016; date of current version July 08, 2016. This work was supported in part by the U.S. Department of Energy Graduate Automotive Technology Education Grant, the U.S.–China Clean Energy Research Center—Clean Vehicle Consortium, DENSO International, San Diego State University, the University of Michigan-Ann Arbor, and the China Scholarship Council. Recommended for publication by Associate Editor R. Zane.

H. Zhang is with the School of Automation, Northwestern Polytechnical University, Xi'an 710072, China, and also with the Department of Electrical and Computer Engineering, San Diego State University, San Diego, CA 92182 USA (e-mail: huazhang@umich.edu).

F. Lu is with the Department of Electrical Engineering and Computer Science, University of Michigan, Ann Arbor, MI 48109 USA, and also with the Department of Electrical and Computer Engineering, San Diego State University, San Diego, CA 92182 USA (e-mail: feilu@umich.edu).

H. Hofmann is with the Department of Electrical Engineering and Computer Science, University of Michigan, Ann Arbor, MI 48109 USA (e-mail: hofmann@umich.edu).

W. Liu is with the School of Automation, Northwestern Polytechnical University, Xi'an 710072, China (e-mail: lwglll@nwpu.edu.cn).

C. C. Mi is with the Department of Electrical and Computer Engineering, San Diego State University, San Diego, CA 92182 USA (e-mail: cmi@sdsu.edu).

Color versions of one or more of the figures in this paper are available online at http://ieeexplore.ieee.org.

Digital Object Identifier 10.1109/TPEL.2016.2520963

I. Introduction

INDUCTIVE power transfer (IPT) has been widely applied in the charging of portable devices [1], [2] and electric vehicles [3]. The efficiency of an IPT system from the dc source to the dc load has reached 96% with 7-kW output power [4], which is already comparable to that of the traditional plug-in charger. However, the drawback of IPT technology lies in its sensitivity to conductive objects, such as metal debris in the air-gap. The magnetic fields generate eddy current losses in the metals nearby the system, causing significant temperature increase, which is dangerous in practice [5].

Capacitive power transfer (CPT) technology is an alternative solution to replace the IPT system. It utilizes electric fields to transfer power, instead of magnetic fields [6]. The electric fields can pass through metal barriers without generating significant power losses. Therefore, the CPT technology is suitable for the electric vehicle charging application [7].

Another advantage of the CPT system is its low cost. In CPT systems, metal plates are used to form capacitors to transfer power [8], [9], while in IPT systems, the coils are made of expensive Litz-wire [10]. The aluminum plate is a cost-efficient option, which has good conductivity, low weight, and low cost.

However, most of the recent CPT systems focus on low-power or short-distance applications, such as the LED driver [11], soccer robot charging [12], and synchronous motor excitation [13]. In particular, the transferred distance is usually around 1 mm, which is far less than the ground clearance of electric vehicles, limiting the application of CPT technology.

This limitation of current CPT systems comes from the circuit topologies working with the coupling capacitors, which are classified into two categories: nonresonant and resonant topologies. The nonresonant topology is a PWM converter, such as the SEPIC converter. The coupling capacitors work as power storage components to smooth the power in the circuit [14]. Therefore, it requires large capacitances, usually in the 10's of nanofarad range, and the transferred distance is less than 1 mm. The resonant topologies include the series resonance converter [15] and the class-E converter [16], in which the coupling capacitors resonate with the inductors in the compensation circuit. The benefit is that the coupling capacitance can be reduced as long as the resonant inductance or the switching frequency is high enough. However, the inductance is limited by its self-resonant

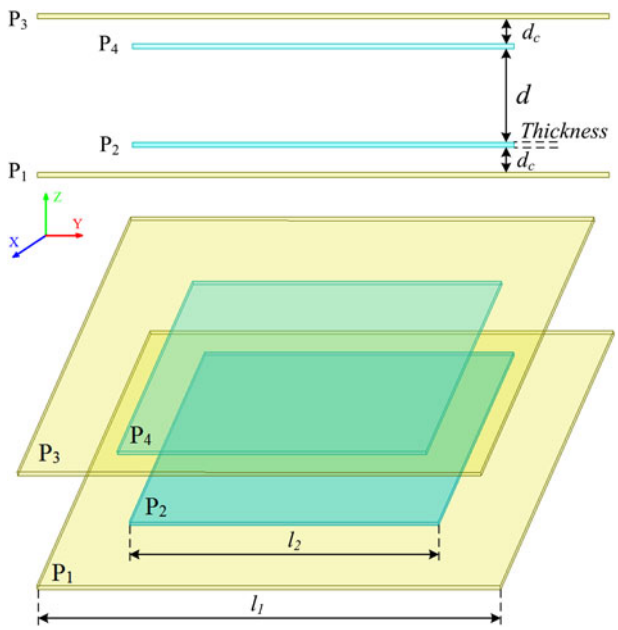

Fig. 1. Structure and dimension of the plates.

frequency [17] and the switching frequency is limited by the efficiency and power capability of the converter [18]. Another problem is that the resonant topology is sensitive to the parameter variations caused by misalignment, which is not acceptable in some critical applications. All these topologies require either too large capacitance or too high switching frequency, which is difficult to realize. Therefore, better circuit topologies need to be proposed for the CPT system.

The double-sided *LCLC*-compensated circuit has been proposed in [7] for high-power and large air gap applications. The transferred distance is 150 mm and the output power reaches 2.4 kW with an efficiency of 91%. Although the coupling capacitor is around 10's of picofarad, there is a 100-pF capacitor connected in parallel with the coupling plates, which reduces the resonant inductor to 100's of microhenry and the switching frequency to 1 MHz. Therefore, the resonances are not affected by parameter variations and misalignments. However, there are eight external components in the compensation network that increase the complexity of the system and are difficult to construct. Also, the two pairs of plates are horizontally separated by 500 mm to eliminate the coupling between the adjacent plates. Therefore, the plates take more space than necessary.

In this paper, a more compact four-plate structure is proposed for the high-power CPT application. In this structure, all the plates are vertically arranged to save space, as shown in Fig. 1. At each side, two plates are placed close to each other to maintain a large coupling capacitance, which is used to replace two external compensation capacitors in the *LCLC* topology. Therefore, the *LCLC* compensation topology can be simplified as the *LCL* topology. To transfer high power through the coupler, it requires generating high voltage between the plates to build up electric fields. For each two plates at the same side, the coupling capacitance can be adjusted through regulating the distance. Then, the switching frequency and system power can be controlled. Since the distance can be reduced to maintain a large capacitance, the system frequency can be reduced to a reasonable range. Also, the capacitance does not relate to the misalignment, so the system has good misalignment ability. The *LCL* topology can resonate with the plates to provide high voltage, and it performs as the constant current source for both the input and output, which is suitable for the battery load.

Another benefit of the vertical structure is its misalignment ability. As shown in Fig. 1, the two plates at the same side are of different sizes, and the outer plate is larger to maintain the coupling with the plates at the other side. For the horizontal structure, the rotary misalignment, which is the mismatch between the primary and secondary plates, can reduce the output power. For the vertical structure, the rotation in the horizontal plane does not cause too much mismatch, and the coupling capacitors remain nearly unchanged. Therefore, it is meaningful to replace the horizontal structure with the proposed vertical one.

Although the vertical structure has been applied in low-power commercial products, there is no overlap between the two plates at the same side. Therefore, the large capacitance considered in this paper is not built into the coupler in [19], which means that the circuit model of [19] is the same as that of the asymmetric horizontal plates. The function of the asymmetric structure is to reduce the voltage stress on the large plate, compared to the small one. The authors in [20] attempt to model a vertical structure with plate overlap, but the Π diagram structure is not sufficient to model the plates. The method of moment is used in [20]. However, it does not provide details, nor does it consider the capacitances between each two plates. The authors in [21] try to introduce the concept of mutual capacitance in the plate model, but the model does not have duality with the classic transformer model, and the capacitances between each two plates are not studied. Therefore, more accurate circuit models of the coupling plates are needed for the CPT system design.

II. Four-Plate Structure and Circuit Model

A. Plate Structure

Fig. 1 illustrates the structure and dimensions of the plates. Both the three-dimensional view and front view are provided. The *XYZ* axis is shown in the figure. The plates are designed to be symmetric from the primary to the secondary side. P_1 and P_2 are embedded on the ground as the power transmitter. P_3 and P_4 are installed on the vehicle as the power receiver. In Fig. 1, P_1 and P_3 are larger than P_2 and P_4. Therefore, the coupling between P_1 and P_3 cannot be eliminated by P_2 and P_4. The plate shape does not affect coupling, so all the plates are designed to be square to simplify the analysis. In the practical application, the plates can be designed to any shape to fit the installation on the vehicle. The only principle is to maintain the area of the plates to transfer sufficient power. The length of P_1 and P_3 is l_1, the length of P_2 and P_3 is l_2, the distance of P_1-P_2 and P_3-P_4 is d_c, and the distance of P_2-P_4 is d, which is the air gap between the primary and secondary side. The thickness of all the plates is the same.

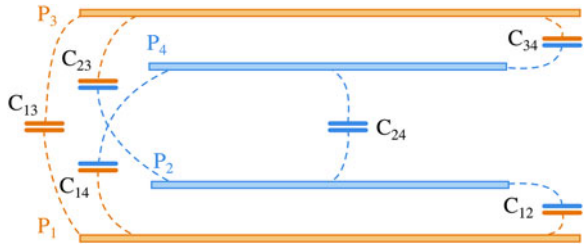

Fig. 2. Coupling capacitors in the plates.

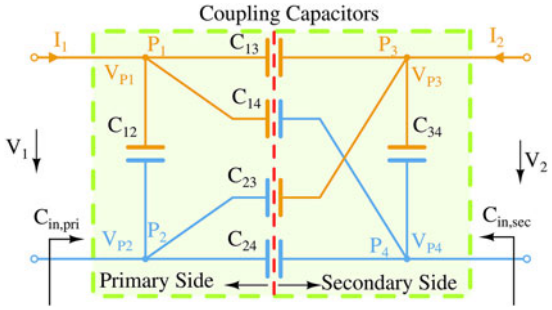

Fig. 3. Circuit model of the coupling capacitors.

B. Circuit Model of the Plates

There is coupling capacitance between each two plates, as shown in Fig. 2. The air gap d is much larger than the plate distance d_c in electric vehicle charging applications, so C_{13} and C_{24} are much smaller than C_{12} and C_{34}. The cross-couplings of C_{14} and C_{23} are generated by the edge effect of P_1–P_4 and P_2–P_3, so they are usually smaller than C_{12} and C_{34}. However, they cannot be neglected in an accurate circuit model. The resulting circuit model of the four-plate vertical structure is shown in Fig. 3. The equivalent input capacitances of the plates from the primary and secondary side are defined as $C_{\mathrm{in,pri}}$ and $C_{\mathrm{in,sec}}$, respectively, which are mainly determined by C_{12} and C_{34}. Since C_{12} and C_{34} are mainly determined by the distance d_c, and they do not relate to the misalignment between the primary and secondary side, so the resonance of this coupler is not sensitive to the misalignment.

In Fig. 3, two independent voltage sources V_1 and V_2 are applied on the plates to derive the relationship between the input and output. All the capacitors correspond to the couplings in Fig. 2. The voltage on each plate is defined as $V_{\mathrm{p}1}$, $V_{\mathrm{p}2}$, $V_{\mathrm{p}3}$, and $V_{\mathrm{p}4}$, respectively. Plate P_2 is selected as the reference, so $V_{\mathrm{p}2}=0$, $V_1=V_{\mathrm{p}1}$, and $V_2=V_{\mathrm{p}3}$–$V_{\mathrm{p}4}$. Therefore, Kirchhoff's current equations are expressed as

$$\begin{cases} (C_{12}+C_{13}+C_{14})\cdot V_{P1}-C_{13}\cdot V_{P3}-C_{14}\cdot V_{P4} \\ \quad = I_1/(j\omega)-C_{12}\cdot V_{P1}-C_{23}\cdot V_{P3}-C_{24}\cdot V_{P4} \\ \quad = -I_1/(j\omega) \\ -C_{13}\cdot V_{P1}+(C_{13}+C_{23}+C_{34})\cdot V_{P3}-C_{34}\cdot V_{P4} \\ \quad = I_2/(j\omega) \\ -C_{14}\cdot V_{P1}-C_{34}\cdot V_{P3}+(C_{14}+C_{24}+C_{34})\cdot V_{P4} \\ \quad = -I_2/(j\omega) \end{cases} \tag{1}$$

where I_1 and I_2 are the currents injected into the plates from the primary and secondary sides, respectively, $\omega=2\pi f_{\mathrm{sw}}$ and f_{sw} is the frequency of the input and output ac sources.

The plates are modeled as a two-port network with V_1 and V_2 as the input and I_1 and I_2 as the output variables. There are four equations in (1), and any three of them are independent. The relationship between voltage and current can be derived from the equations in (1). Considering the first two equations in (1), $V_{\mathrm{P}3}$ and $V_{\mathrm{P}4}$ can be eliminated, as follows:

$$\begin{cases} [C_{24}(C_{12}+C_{13}+C_{14})+C_{12}C_{14}]\cdot V_{P1} \\ \quad -(C_{13}C_{24}-C_{14}C_{23})\cdot V_{P3}=(C_{24}+C_{14})I_1/(j\omega) \\ [C_{23}(C_{12}+C_{13}+C_{14})+C_{12}C_{13}]\cdot V_{P1} \\ \quad +(C_{13}C_{24}-C_{14}C_{23})\cdot V_{P4}=(C_{23}+C_{13})I_1/(j\omega) \end{cases}. \tag{2}$$

Since $V_1=V_{\mathrm{P}1}$ and $V_2=V_{\mathrm{P}3}$–$V_{\mathrm{p}4}$, the relationship between V_1, I_1, and V_2 can be expressed as

$$V_1=I_1\cdot\frac{1}{j\omega\left[C_{12}+\frac{(C_{13}+C_{14})\cdot(C_{23}+C_{24})}{C_{13}+C_{14}+C_{23}+C_{24}}\right]}+ V_2\cdot\frac{C_{24}C_{13}-C_{14}C_{23}}{C_{12}\cdot(C_{13}+C_{14}+C_{23}+C_{24})+(C_{13}+C_{14})\cdot(C_{23}+C_{24})}. \tag{3}$$

Similarly, using the other two equations in (1), the relationship between V_2, I_2, and V_1 can be expressed as

$$V_2=I_2\cdot\frac{1}{j\omega\left[C_{34}+\frac{(C_{13}+C_{23})\cdot(C_{14}+C_{24})}{C_{13}+C_{14}+C_{23}+C_{24}}\right]}+ V_1\cdot\frac{C_{24}C_{13}-C_{14}C_{23}}{C_{34}\cdot(C_{13}+C_{14}+C_{23}+C_{24})+(C_{13}+C_{23})\cdot(C_{14}+C_{24})}. \tag{4}$$

From (3) and (4), the capacitances C_1, C_2, and C_{M} can be defined as

$$\begin{cases} C_1=C_{12}+\dfrac{(C_{13}+C_{14})\cdot(C_{23}+C_{24})}{C_{13}+C_{14}+C_{23}+C_{24}} \\ C_2=C_{34}+\dfrac{(C_{13}+C_{23})\cdot(C_{14}+C_{24})}{C_{13}+C_{14}+C_{23}+C_{24}} \\ C_M=\dfrac{C_{24}C_{13}-C_{14}C_{23}}{C_{13}+C_{14}+C_{23}+C_{24}} \end{cases}. \tag{5}$$

Therefore, (3) and (4) can be rewritten as

$$\begin{cases} V_1=I_1\cdot\dfrac{1}{j\omega C_1}+V_2\cdot\dfrac{C_M}{C_1} \\ V_2=I_2\cdot\dfrac{1}{j\omega C_2}+V_1\cdot\dfrac{C_M}{C_2} \end{cases}. \tag{6}$$

Moving I_1 and I_2 to the left-hand side, the relationship between the current and the voltage is

$$\begin{cases} I_1=j\omega C_1\cdot V_1-j\omega C_M\cdot V_2 \\ I_2=j\omega C_2\cdot V_2-j\omega C_M\cdot V_1 \end{cases}. \tag{7}$$

According to (7), the simplified equivalent model of coupling capacitors with behavior sources is shown in Fig. 4(a). Each of the two current sources depends on the voltage at the other side and they are separated by a dashed line.

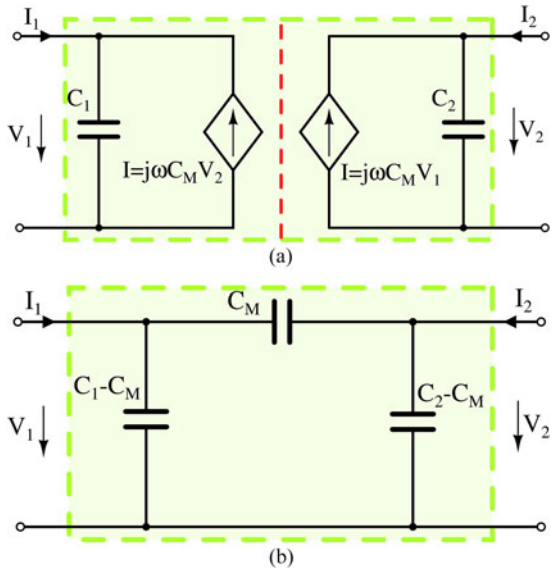

Fig. 4. Simplified equivalent model of coupling capacitors. (a) Behavior source model. (b) π model.

Equation (7) is further written as (8). Then, the equivalent model of the capacitors is simplified to a π shape, as shown in Fig. 4(b). This model is suitable to simplify the parameter calculation in the circuit. It needs to be emphasized that the primary and secondary sides are not separated in the π shape model

$$\begin{cases} I_1 = j\omega(C_1 - C_M)\cdot V_1 + j\omega C_M \cdot (V_1 - V_2) \\ I_2 = j\omega(C_2 - C_M)\cdot V_2 + j\omega C_M \cdot (V_2 - V_1) \end{cases}. \tag{8}$$

Similar to that of the coils, the capacitive coupling coefficient k_c of the plates is defined with the parameters from (5), as follows:

$$k_C = \frac{C_M}{\sqrt{C_1 \cdot C_2}} = \frac{\sqrt{C_{24}C_{13} - C_{14}C_{23}}}{\sqrt{C_{12}(C_{13}+C_{14}+C_{23}+C_{24}) + (C_{13}+C_{14})(C_{23}+C_{24})}} \cdot \frac{\sqrt{C_{24}C_{13} - C_{14}C_{23}}}{\sqrt{C_{34}(C_{13}+C_{14}+C_{23}+C_{24}) + (C_{13}+C_{23})(C_{14}+C_{24})}}. \tag{9}$$

From the simplified model in Fig. 4, the self-capacitance of the primary side is C_1, the self-capacitance of the secondary side is C_2, the mutual capacitance between the primary and secondary is C_{M}, and the capacitive coupling coefficient is k_{c}.

For the horizontal structure in [7], the plates at the same side are placed 500 mm away, so the coupling capacitance C_{12} and C_{34} are both close to zero. Cross-coupling capacitances C_{14} and C_{23} are also close to zero. As a result, the capacitive coupling coefficient is $k_{\mathrm{c}} \approx 1$.

For the vertical structure shown in Fig. 2, the plate distance d_{c} is much smaller than the air gap distance d, so C_{12} and C_{34} are much larger than C_{13} and C_{24}. As a result, the capacitive coupling coefficient $k_c \ll 1$, which means it is a loosely coupled CPT system.

Since the plates work as a single capacitor to resonate with the inductor in the circuit, it is important to calculate the equivalent input capacitances of the plates. Fig. 3 shows the capacitances $C_{\mathrm{in,pri}}$ and $C_{\mathrm{in,sec}}$ from the primary and secondary sides, respectively. It is convenient to use the simplified capacitor model in Fig. 4 to perform the calculations. Therefore, the equivalent input capacitances are

$$\begin{cases} C_{\mathrm{in,pri}} = \left.\dfrac{I_1}{j\omega \cdot V_1}\right|_{I_2=0} = C_1 - C_M + \dfrac{C_M(C_2 - C_M)}{C_2} \\ \qquad\qquad = (1-k_c^2)C_1 \\ C_{\mathrm{in,sec}} = \left.\dfrac{I_2}{j\omega \cdot V_2}\right|_{I_1=0} = C_2 - C_M + \dfrac{C_M(C_1 - C_M)}{C_1} \\ \qquad\qquad = (1-k_c^2)C_2 \end{cases}. \tag{10}$$

The transfer function between the input and output voltage is also an important parameter to determine the amount of the transferred power. The voltage transfer function from the primary to the secondary side is defined as $H_{1,2}$ and the voltage transfer function from the secondary to the primary is defined as $H_{2,1}$. They are expressed as

$$\begin{cases} H_{1,2} = \left.\dfrac{V_2}{V_1}\right|_{I_2=0} = \dfrac{C_M}{C_2} = k_c\sqrt{\dfrac{C_1}{C_2}} \\ H_{2,1} = \left.\dfrac{V_1}{V_2}\right|_{I_1=0} = \dfrac{C_M}{C_1} = k_c\sqrt{\dfrac{C_2}{C_1}} \end{cases}. \tag{11}$$

The plate model in Fig. 4 includes the voltage stress between plates P_1 and P_2 and the stress between P_3 and P_4. However, it does not consider the voltage between P_1 and P_3, or the voltage between P_2 and P_4, which are also important in the system design. Since P_2 is set to be the reference, the second equation in (2) is used to calculate the voltage between P_2 and P_4, as follows:

$$V_{P4-P2} = V_{P4} = \frac{(C_{23}+C_{13})\cdot I_1}{j\omega(C_{13}C_{24} - C_{23}C_{14})} - \frac{C_{12}(C_{13}+C_{23}) + C_{23}(C_{13}+C_{14})}{(C_{13}C_{24} - C_{23}C_{14})} \cdot V_1. \tag{12}$$

Using (1), the voltage between P_1 and P_3 is expressed as

$$V_{P1-P3} = V_{P1} - V_{P3} = \frac{-(C_{23}+C_{24})\cdot I_2}{j\omega(C_{13}C_{24} - C_{23}C_{14})} + \frac{C_{34}(C_{23}+C_{24}) + C_{23}(C_{14}+C_{24})}{(C_{13}C_{24} - C_{23}C_{14})} V_2. \tag{13}$$

C. Plate Dimensions Design

Using the circuit model of the plates, the dimensions of the plates can be determined for the electric vehicle charging application. All the variables are shown in Fig. 1. The purpose of the dimension design is to calculate all the capacitances in (5)

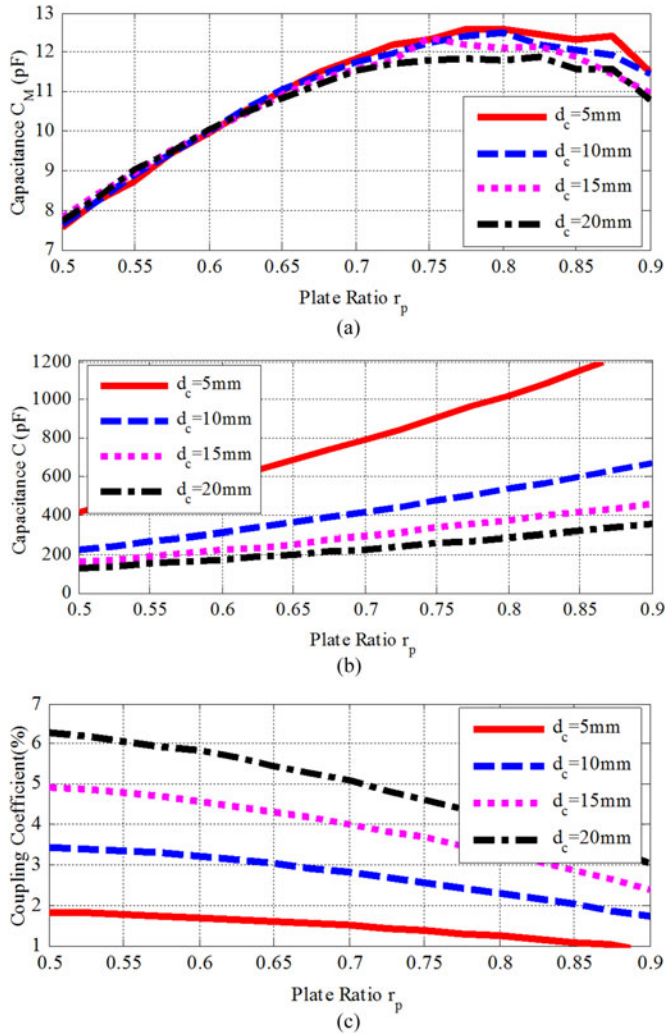

Fig. 5. Plates parameters at different r_p and d_c, when $l_1 = 914$ mm, $d = 150$ mm. (a) Capacitance C_M. (b) Capacitance C. (c) Coupling Coefficient k_C.

and analyze the behavior of the plates. Since the plate structure is designed to be symmetric from the primary to the secondary side, C is defined as $C = C_1 = C_2$.

Considering the space limitation, the length l_1 of P_1 and P_3 is 914 mm. The air gap is set to be 150 mm, which is the ground clearance of the electric vehicle. Therefore, there are only two parameters, d_c and l_2, that need to be designed. The plate ratio r_p is defined as $r_p = l_2/l_1$.

The plate structure in Fig. 2 is much more complex than the parallel plates in [22]. Since the cross coupling is usually small, it can be neglected at the beginning stage of the plates design. The empirical formula of parallel plates in [22] can be used to estimate the capacitance based on the system dimensions to accelerate the design process. This estimation can provide a reasonable range of the dimensions. Then, the finite-element analysis (FEA) by Maxwell can be used to accurately determine the final dimensions and the corresponding circuit model of the plates.

The FEA simulation provides a capacitance matrix with all the six mutual capacitors in Fig. 2. Using the capacitance matrix,

TABLE I
CAPACITANCE VALUES OF PLATES, WHEN $l_1 = 914$ MM, $l_2 = 610$ MM, $d_c = 10$ MM, AND $d = 150$ MM

Parameter	Value	Parameter	Value
C_{12}	365.7 pF	C_{34}	365.7 pF
C_{13}	42.40 pF	C_{24}	19.52 pF
C_{14}	4.72 pF	C_{23}	4.72 pF
C_1	380.9 pF	C_2	380.9 pF
C_M	11.3 pF	k_C	2.90%

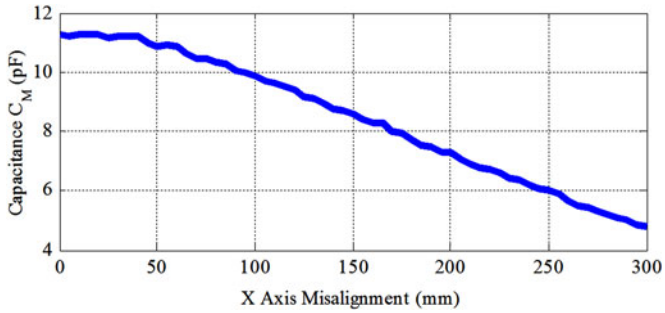

Fig. 6. Mutual capacitance C_M, at X misalignment conditions.

the equivalent capacitances C and C_M are further calculated according to (5), and the capacitive coupling coefficients are obtained from (9). When the plate ratio r_p and distance d_c vary, all the plate capacitances are analyzed in Maxwell. The equivalent parameters (C_M, C, and k_C) in the plate model are shown in Fig. 5 as the function of r_p and d_c.

Fig. 5(a) shows that the mutual capacitance C_M is only sensitive to the plate ratio r_p. Fig. 5(b) shows that the increase of r_p and the decrease of d_c both cause the increase of the self-capacitance C. For the capacitive coupling coefficient k_C, Fig. 5(c) shows that it is smaller than 10%, which indicates that it is a loosely coupled CPT system.

According to [7], there is an external inductor resonating with the self-capacitance. The self-capacitance should be large enough to reduce the inductor's value and volume. At the same time, the coupling coefficient should be large enough to maintain the system power as well. Therefore, considering Fig. 5(b) and (c), the plate distance d_c is set to be 10 mm and the plate ratio r_p is 0.667. All the capacitances for this scenario are shown in Table I.

The misalignment ability of the plates is also analyzed in Maxwell. When there is a rotation of the secondary plates in the horizontal plane as shown in Fig. 1, the variation of self-capacitance $C_{1,2}$ is within 1% of the well-aligned value and the variation of the mutual capacitance C_M is within 10%. When there is displacement misalignment, the variation of the self-capacitance is negligible, and the variation of the mutual inductance is shown in Fig. 6. The X axis is as defined in Fig. 1. This figure shows that C_M can maintain higher than 50% of the nominal value when the misalignment increases to 250 mm.

III. DOUBLE-SIDED *LCL* COMPENSATION TOPOLOGY

A double-sided *LCL* compensation circuit is proposed to work with the plates, as shown in Fig. 7. The plates are in the vertical

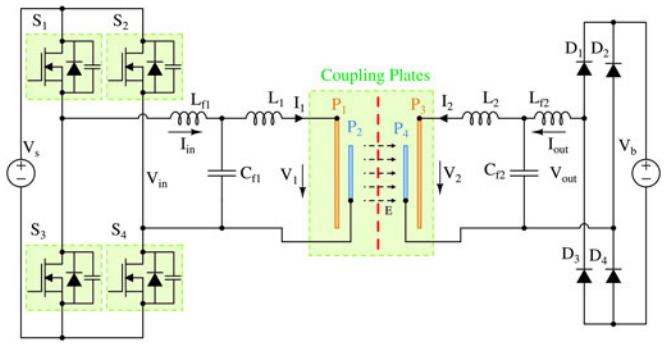

Fig. 7. Double-sided *LCL* compensated circuit topology.

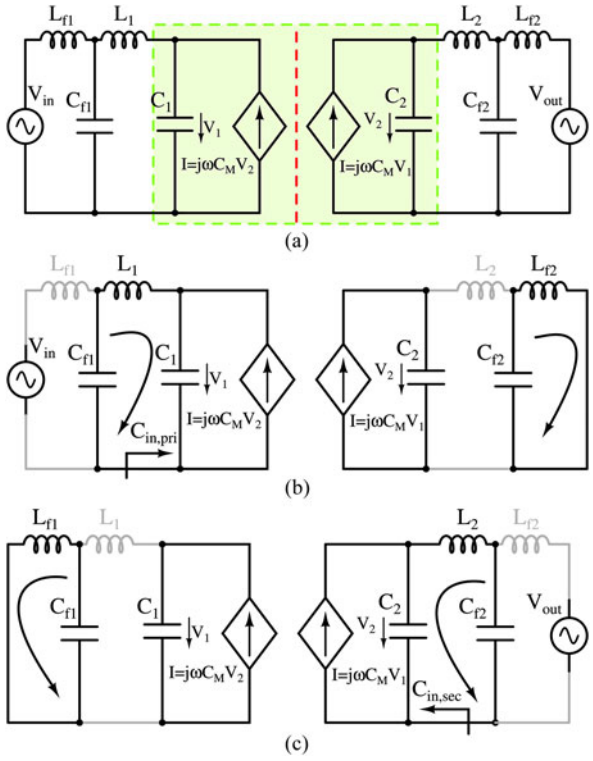

Fig. 8. FHA analysis of the CPT system. (a) Simplified circuit model. (b) Excited only by primary source. (c) Excited only by secondary source.

structure as shown in Fig. 2. There are multiple resonances in the circuit. At the primary side, there is a full-bridge inverter, generating excitation $V_{\rm in}$ to the resonant tank. At the secondary side, a full-bridge rectifier is used to provide the dc current to the output battery. In Fig. 7, all the components are assumed to have a high quality factor, and the parasitic resistances are neglected in the analysis process.

L_{f1} and C_{f1} work as a low-pass filter at the front end. Similarly, L_{f2} and C_{f2} work as a low-pass filter at the back end. Therefore, there is no high-order harmonics current injected into the plates. The fundamental harmonics approximation (FHA) method is used to analyze the working principle of the system. Fig. 8(a) shows the simplified circuit topology of the CPT system with the equivalent circuit model of the plates in Fig. 4(a). The input and output square-wave sources are represented by two sinusoidal ac sources. Since the circuit in Fig. 8(a) is linear, the superposition theorem is used to analyze the two ac sources separately, as shown in Fig. 8(b) and (c).

Fig. 8(b) shows that the resonant circuit is excited only by the primary source. L_{f2} and C_{f2} form a parallel resonance, and their impendance is infinite. L_2 is treated as an open circuit. L_1, C_{f1}, and $C_{\rm in,pri}$ form another parallel resonance, so there is no current flowing through L_{f1}, which means that the input current does not rely on the input voltage $V_{\rm in}$. Therefore, the relationship between the circuit parameters is

$$\begin{cases} \omega = 2\pi f_{\rm sw} = 1/\sqrt{L_{f2}C_{f2}} \\ L_1 = 1/(\omega^2 C_{f1}) + 1/(\omega^2 C_{\rm in,pri}) \end{cases}. \tag{14}$$

The output current depends on the input voltage. Since L_{f1} and L_2 are treated as open circuits, $V_{\rm Cf1} = V_{\rm in}$, $V_{\rm Cf2} = V_2$. The transfer function between the primary and secondary voltages in (11) is used to calculate the voltage and current. Therefore, the output current is calculated as

$$\begin{cases} V_1 = V_{\rm Cf1} \cdot \dfrac{C_{f1}}{C_{\rm in,pri}} = V_{\rm in} \cdot \dfrac{C_{f1}}{(1-k_C^2)C_1} \\ V_2 = H_{1,2} \cdot V_1 = \dfrac{C_M \cdot C_{f1} \cdot V_{\rm in}}{(1-k_C^2)\cdot C_1 C_2} \\ I_{\rm Lf2} = V_2 \cdot \dfrac{1}{j\omega L_{f2}} = V_2 \cdot \dfrac{\omega \cdot C_{f2}}{j} \\ \qquad = \dfrac{\omega \cdot C_M \cdot C_{f1}C_{f2} \cdot V_{\rm in}}{j(1-k_C^2)\cdot C_1 C_2} \end{cases}. \tag{15}$$

There is a full-brige rectifier at the secondary side, so the output voltage and current are in phase. Fig. 8(c) indicates that the output voltage does not affect the output current. Therefore, the output power can be expressed as

$$P_{\rm out} = |V_{\rm out}| \cdot |I_{\rm Lf2}| = \frac{\omega \cdot C_M \cdot C_{f1}C_{f2}}{(1-k_C^2)\cdot C_1 C_2} \cdot |V_{\rm in}| \cdot |V_{\rm out}|. \tag{16}$$

Fig. 8(c) shows that the resonant circuit is excited only by the secondary source. Similar to the analysis of Fig. 8(b), there are two parallel resonances. L_{f1} and C_{f1} form one resonance, and L_2, C_{f2}, and $C_{\rm in,sec}$ form the other resonance. Because of the infinite impendance of the parallel resonance, L_1 and L_{f2} are treated as open circuits. The input current depends only on the output voltage. Therefore, the relationship between the circuit parameters is

$$\begin{cases} \omega = 2\pi f_{sw} = 1/\sqrt{L_{f1}C_{f1}} \\ L_2 = 1/(\omega^2 C_{f2}) + 1/(\omega^2 C_{\rm in,sec}) \end{cases}. \tag{17}$$

The input current depends on the output voltage. Since L_1 and L_{f2} are open circuits, then $V_{\rm Cf1} = V_1$, $V_{\rm Cf2} = V_{\rm out}$. Considering the equivalent capacitance $C_{\rm in,sec}$ in (10) and the voltage transfer function $H_{2,1}$ in (11), the input current can be calculated as

$$\begin{cases} V_2 = V_{\rm Cf2} \cdot \dfrac{C_{f2}}{C_{\rm in,sec}} = V_{\rm out} \cdot \dfrac{C_{f2}}{(1-k_C^2)C_2} \\ V_1 = H_{2,1} \cdot V_2 = \dfrac{C_M \cdot C_{f2} \cdot V_{\rm out}}{(1-k_C^2)\cdot C_1 C_2} \\ I_{\rm Lf1} = V_1 \cdot \dfrac{1}{j\omega L_{f1}} = V_1 \cdot \dfrac{\omega \cdot C_{f1}}{j} = \dfrac{\omega \cdot C_M \cdot C_{f1}C_{f2} \cdot V_{\rm out}}{j(1-k_C^2)\cdot C_1 C_2} \end{cases}. \tag{18}$$

TABLE II
VOLTAGE STRESS ON CIRCUIT COMPONENTS

Component	Voltage Stress
L_{f1}, L_{f2}	$V_{\mathrm{Lf1}} = \frac{C_M \cdot C_{f2} \cdot V_{\mathrm{out}}}{(1-k_C^2)\cdot C_1 C_2}, V_{\mathrm{Lf2}} = \frac{C_M \cdot C_{f1} \cdot V_{\mathrm{in}}}{(1-k_C^2)\cdot C_1 C_2}$
C_{f1}, C_{f2}	$V_{\mathrm{Cf1}} = V_{\mathrm{in}} + V_{\mathrm{Lf1}}, V_{\mathrm{Cf2}} = V_{\mathrm{out}} + V_{\mathrm{Lf2}}$
L_1, L_2	$V_{L1} = \omega^2 L_1 C_{f1} \cdot V_{\mathrm{in}}, V_{L2} = \omega^2 L_2 C_{f2} \cdot V_{\mathrm{out}}$
P_1–P_2	$V_{P1-P2} = \frac{C_{f1} \cdot V_{\mathrm{in}}}{(1-k_C^2)\cdot C_1} + \frac{C_M C_{f2} \cdot V_{\mathrm{out}}}{(1-k_C^2)\cdot C_1 C_2}$
P_3–P_4	$V_{P3-P4} = \frac{C_M C_{f1} \cdot V_{\mathrm{in}}}{(1-k_C^2)\cdot C_1 C_2} + \frac{C_{f2} \cdot V_{\mathrm{out}}}{(1-k_C^2)\cdot C_2}$
P_1–P_3	$\frac{C_{34}(C_{23}+C_{24})+C_{23}(C_{14}+C_{24})}{(C_{13}C_{24}-C_{23}C_{14})} V_{P3-P4}$ $-\frac{(C_{23}+C_{24})C_{f2}V_{\mathrm{out}}}{(C_{13}C_{24}-C_{23}C_{14})}$
P_2–P_4	$\frac{(C_{23}+C_{13})C_{f1}V_{\mathrm{in}}}{(C_{13}C_{24}-C_{23}C_{14})}$ $-\frac{C_{12}(C_{13}+C_{23})+C_{23}(C_{13}+C_{14})}{(C_{13}C_{24}-C_{23}C_{14})} V_{P1-P2}$

Equation (18) shows that I_{Lf1} is 90° lagging V_{out}, and (15) shows that I_{Lf2} is 90° lagging V_{in}. Since V_{out} and I_{Lf2} are in phase, I_{Lf1} is 180° lagging V_{in}. The input current direction is opposite to that of I_{Lf1}, so it is in phase with V_{in}. Therefore, the input power is expressed as

$$P_{\mathrm{in}} = |V_{\mathrm{in}}| \cdot |-I_{\mathrm{Lf1}}| = \frac{\omega \cdot C_M \cdot C_{f1} C_{f2}}{(1-k_C^2)\cdot C_1 C_2} \cdot |V_{\mathrm{in}}| \cdot |V_{\mathrm{out}}|. \tag{19}$$

A comparison of (16) and (19) shows that when the parasitic resistances are neglected, the input and output power are the same, which also supports the previous assumption.

Equation (19) shows that the system power is propotional to the mutual capacitance C_M, the filter capacitances $C_{f1,2}$, the voltage V_{in} and V_{out}, and the switching frequency f_{sw}. According to the plate design in Section II, the capacitive coupling coefficient k_C is usually much smaller than 10%, so $(1 - {k_C}^2) \approx 1$. Therefore, the system power can be simplified as

$$P_{\mathrm{in}} = P_{\mathrm{out}} \approx \frac{\omega \cdot C_M \cdot C_{f1} C_{f2}}{C_1 C_2} \cdot |V_{\mathrm{in}}| \cdot |V_{\mathrm{out}}|. \tag{20}$$

Considering the input dc voltage V_s and the output battery voltage V_b in Fig. 7, (20) can be rewritten

$$P_{\mathrm{in}} = P_{\mathrm{out}} \approx \frac{\omega \cdot C_M \cdot C_{f1} C_{f2}}{C_1 C_2} \cdot \frac{2\sqrt{2}}{\pi} V_s \cdot \frac{2\sqrt{2}}{\pi} V_b. \tag{21}$$

In the high-power CPT system, the voltage stress on the circuit component, especially the metal plates, is an important concern. The voltage on inductors $L_{f1,2}, L_{1,2}$ and capacitors $C_{f1,2}$ can be calculated using the current flowing through them. The voltage between two plates can be calculated according to (12), (13), (15), and (18), which are shown in Table II.

IV. PROTOTYPE DESIGN

After the plate structure and *LCL* compensation circuit topology have been proposed, a prototype of the CPT system is designed. According to (14), (17), and (19), all the circuit parameters are designed as shown in Table III.

TABLE III
SYSTEM SPECIFICATIONS AND CIRCUIT PARAMETER VALUES

Parameter	Design Value	Parameter	Design Value
V_{in}	270 V	V_{out}	270 V
l_1	914 mm	l_2	610 mm
d_c	10 mm	r_p	0.667
f_{sw}	1 MHz	C_M	11.3 pF
L_{f1}	2.90 μH	L_{f2}	2.90 μH
C_{f1}	8.73 nF	C_{f2}	8.73 nF
L_1	69.4 μH	L_2	70.0 μH
C_1	380.9 pF	C_2	380.9 pF

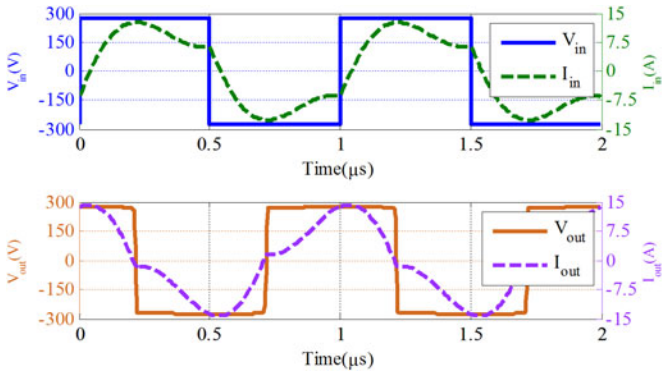

Fig. 9. Simulated input and output voltage and current waveforms.

TABLE IV
RMS VALUE OF THE VOLTAGE STRESS ON EACH COMPONENT

Parameter	Voltage	Parameter	Voltage
V_{Lf1}	211 V	V_{Lf2}	211 V
V_{Cf1}	277.5 V	V_{Cf2}	330.5 V
V_{L1}	5.34 kV	V_{L2}	5.36 kV
V_{P1-P2}	5.12 kV	V_{P3-P4}	5.08 kV
V_{P1-P3}	2.44 kV	V_{P2-P4}	5.29 kV

Because of the symmetry of the plate structure, the other circuit parameters are also designed to be symmetric. Considering the limitation of the semiconductor devices, the switching frequency is 1 MHz. This circuit topology is similar to the *LCLC* compensation topology in [7], and L_2 is larger than L_1 to provide soft-switching condition to the input inverter.

The CPT system is simulated in LTspice with the parameter values in Table III. The simulated waveforms of the CPT system are shown in Fig. 9. The input voltage V_{in} is almost in phase with the input current I_{in}. The cutoff current at the switching transient is about 6 A, which is enough to provide soft-swithing condition to the switches. The input voltage is 90° lagging the output voltage V_{out}, which coincides with the FHA analysis in Secion III.

The RMS value of the voltage stress on each component is calculated using Table II, which also agrees with the LTspice simulation. The simulated results are shown in Table IV. It

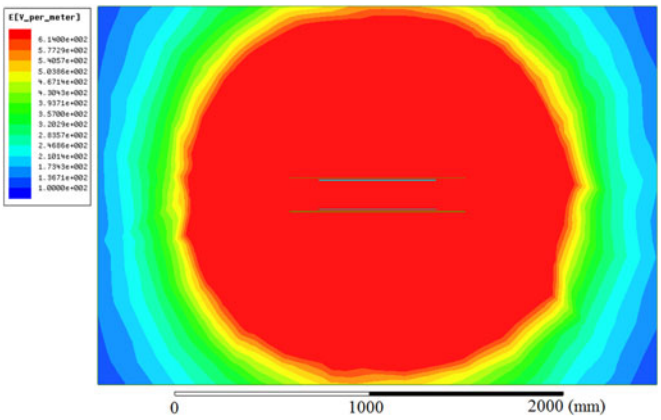

Fig. 10. Electric fields distribution of the plates.

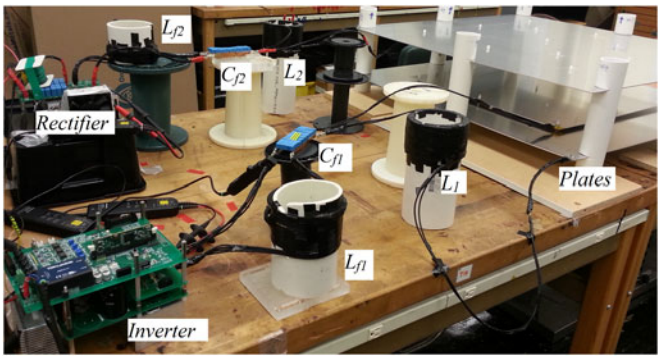

Fig. 11. Prototype of the CPT system with the vertical plate structure.

shows that the voltage stress on the filter component is relatively low. However, the voltage stress on inductor $L_{1,2}$ is higher than 5 kV, so the insulation between each turn of the inductor should be considered in the manufacturing process. The voltage between P_1 and P_2 is 5.12 kV, and the plate distance $d_c = 10$ mm. The breakdown voltage of air is about 3 kV/mm. Therefore, there is no concern of arcing.

The radiation of the leakage electric flux is an important safety concern in the high-power CPT system. The electric fields around the plates can be analyzed by Maxwell, using the voltage stresses in Table IV. The simulation result is shown in Fig. 10. To simplify the simulation, only the four metal plates are considered, and the vehicle structure is neglected. According to the IEEE standard, the leakage electric field should be lower than 614 V/m at 1 MHz due to the human safety concern [23]. The simulation result indicates that the required safety distance for this system is about 1 m. Future research will optimize the plate structure to reduce the leakage electric fields.

V. Experimental Results

A. Experiment Setup

With the parameters in Table III, a CPT system prototype is constructed as shown in Fig. 11. Four aluminum plates are vertically arranged to form the capacitive coupler. The ceramic

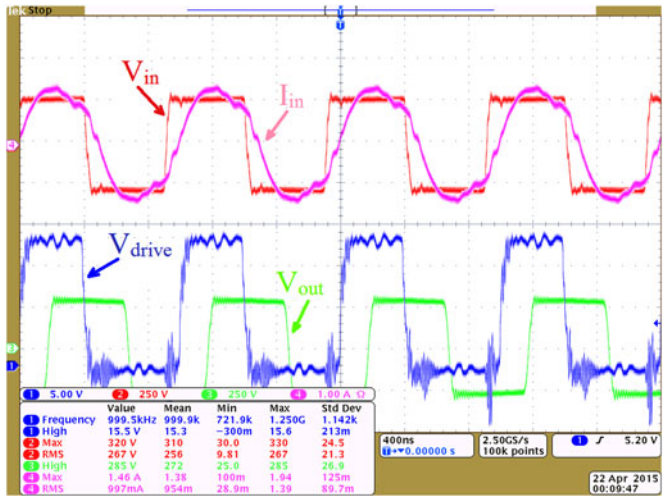

Fig. 12. Experimental input and output waveforms.

spacers are used to separate the inner and outer plates at the same side. The white PVC tubes are used to hold the plates as shown in Fig. 11. The skin depth of copper is 65 μm at 1 MHz, so the AWG 46 Litz-wire with the diameter of 40 μm is used to make the inductors and reduce the skin effect losses. Since the inductors are air-cored and wound on PVC tubes, the magnetic losses are eliminated. High-power and high-frequency polypropylene thin-film capacitors from KEMET are used to resonate with the inductor, and the dissipation factor is 0.18% at 1 MHz. The connections between the inductors, capacitors, and plates are also shown in Fig. 11, in which the components are connected to the edge of the plates.

Silicon Carbide (SiC) MOSFETs C2M0080120D from CREE are used in the input inverter. The datasheet shows that the output parasitic capacitance between drain and source is 110 pF at 270 V. As mentioned in Section IV, the MOSFETs can achieve zero-voltage-switching, and only the conduction losses are considered. The output rectifier utilizes SiC Diode IDW30G65C from Infineon, and the forward voltage of the diode is used to estimate the power losses.

B. Experimental Results

The experimental waveforms, which are similar to those of the simulation results in Fig. 9, are shown in Fig. 12. The input voltage and current are almost in phase with each other. $V_{\rm out}$ is 180° inverted, so it is lagging $V_{\rm in}$ in Fig. 9. The switch current at the switching transient is about 6 A, and the zero-voltage-switching conditon is achieved. There is noise on the driver signal at the switching transient. However, the magnitude of the noise is within 3V, which is lower than the threshold voltage of the SiC MOSFET, so it is still acceptable for the safe operation of the MOSFETs.

When the input and ouput voltages increase, the relationship betwteen output power and efficiency is shown in Fig. 13. It shows that the system efficiency keeps increasing with the increase of the output power. For the no misalignment case, the system can maintain an efficiency higher than 85% when the

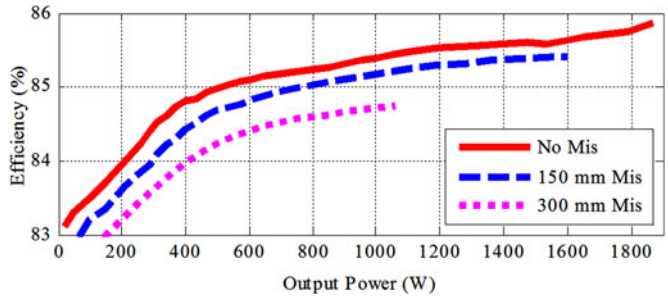

Fig. 13. System output power and efficiency at different misalignments.

power is higher than 600 W. When the input and output voltages are both 270 V, the system input power reaches maximum to 2.17 kW. The output power is 1.88 kW with the efficiency of 85.87%.

The misalignment ability of the prototype is also tested as shown in Fig. 13. The misalignement is in *X* axis in the horizontal plane as shown in Fig. 1. The maximum load ability decreases with the misalignments. When there is 15-cm misalignment between the primary and secondary plates, the maximum output power of the system drops to 1.60 kW with the efficiency of 85.42%. When the misalignment increases to 30 cm, the maximum output power drops to 1.06 kW with the efficeincy of 84.74%. At the maximum misalignment of 30 cm, the system power drops to about 56.4% of the well aligned case. The rotatory misalignemnt test is also conducted, in which the primary plates are fixed and the secondary plates are rotated in the horizontal plane to different angles. In this experiment, the system output power is maintained and the power ripple is within $\pm 5.0\%$ of the nominal power. It shows that this system has good misalignment ability to the horizontal plane rotation.

The distribution of the power losses in the circuit components is also estimated for the prototype. The circuit components' models discussed in [24] and [25] are used to calculte the power losses. For all the inductors, the ac resistance at 1 MHz is 3.4 times of the dc resistance. For all the capacitors, the parasitic resistance is calculated according to the dissipation factor, which is 0.18% at 1 MHz. For the MOSFETs in the inverter, they work under soft-switching condition, so only the conduction losses are considered. For the diodes in the rectifier, the forward voltage is used to calculate the losses. With all these models, the remaining losses are estimated to be from the coupling plates. Therefore, the power loss distribution is shown in Fig. 14.

It shows that 43% of the power consumptions are in the inductors L_1 and L_2. The aluminum plates dissipate 36% of the total power losses. Considering the loss distribution, the structure of the inductors and plates need to be optimized to reduce the total power loss in future research.

C. Discussion and Comparison With LCLC Compensation

The experimental results of this *LCL*-compensated CPT system with vertically arranged plates are compared with the previous published *LCLC*-compensated CPT system with horizontally arranged plates in [7]. The *LCL* system has better misalignment ability to rotation, and the *LCLC* system has

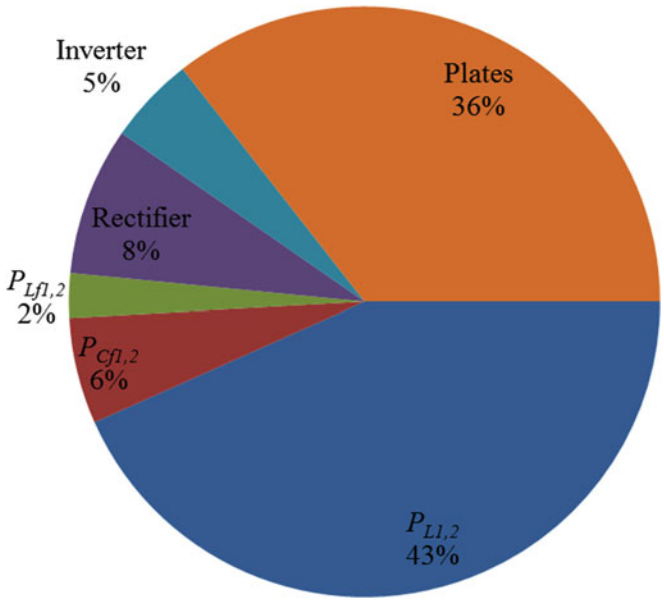

Fig. 14. Power loss distribution of the components.

better ability to the displacement misalignment. When there is 90° rotation between the primary and secondary plates, the *LCL* system can maintain the original power, and the power in the *LCLC* system drops dramatically. When there is 30-cm displacement between the plates, the *LCLC* system can maintain 87.5% of the origianl power, and the power in the *LCL* system drops to 56.4%. Therefore, the proposed vertical arranged plates structure is more original for the situation where the rotatory misalignment is unavoidable and significant.

The experiments also show that the efficiency of the *LCLC* system in [7] is about 5% higher than the *LCL* system proposed in this paper. It is because there is more power dissipated in the two inductors L_1 and L_2. For a given system, the power loss distribution relates to the parameter values. Compared to the *LCLC* system, although the inductances L_1 and L_2 are reduced, the currents flowing through them are increased. Therefore, all the power losses in the components need to be considered together. In future research, the system efficiency will be optimized through designing the parameter values.

The power transfer density is also an important specification to evaluate the CPT system. For the *LCL*-compensated system in this paper, its power transfer density is calculated as

$$P_{D,\mathrm{LCL}} = \frac{P_{\mathrm{out}}}{l_1^2} = \frac{1.88\,\mathrm{kW}}{0.914^2\,\mathrm{m}^2} = 2.25\,\mathrm{kW/m}^2. \tag{22}$$

For the *LCLC*-compensated system in [7], the space between the two pairs of plates should be considered, so its power transfer density is calculated as

$$P_{D,\mathrm{LCLC}} = \frac{P_{\mathrm{out}}}{l \cdot (2l + d_1)} = \frac{2.4\,\mathrm{kW}}{0.61 \cdot (2 \times 0.61 + 0.5)\mathrm{m}^3} = 2.29\,\mathrm{kW/m}^2. \tag{23}$$

The power transfer density of the IPT system is also compared. For the *LCC*-compensated IPT system in [24], its power

transfer density is calculated as

$$P_{D,\mathrm{IPT}} = \frac{P_{\mathrm{out}}}{l_1 \cdot l_2} = \frac{5.7\,\mathrm{kW}}{0.60 \cdot 0.80\,\mathrm{m}^2} = 11.88\,\mathrm{kW/m}^2. \quad (24)$$

It shows that the power transfer density of these two CPT systems is comparable, and the IPT system has much higher power transfer density than the CPT system. In future research, the power density of the CPT system can be improved by increasing the voltage on the plates. Meanwhile, the safety and radiation issues should be considered in the system design.

VI. Conclusion

This paper proposed a vertical structure of plates and the corresponding *LCL* compensation circuit topology for high-power CPT. The equivalent circuit model of the plates is derived using the coupling capacitance between two plates. The circuit model is described by a voltage-controlled current source, which is the duality of the classic transformer model. The voltage and current of each component are calculated using the FHA method, with which the system power is derived. A prototype of the CPT system is designed and built to validate the proposed plate structure and compensation circuit topology. The system efficiency reaches 85.87% with 1.87-kW output power and a 150-mm air gap. Future research will focus on the study of electric fields radiation to make the proposed system safer for use in the electric vehicle charging application.

References

[1] C.-G. Kim, D.-H. Seo, J.-S. You, J.-H. Park, and B. H. Cho, "Design of a contactless battery charger for cellular phone," *IEEE Trans. Ind. Electron.*, vol. 48, no. 6, pp. 1238–1247, Dec. 2001.

[2] S. Raabe and G. A. Covic, "Practical design considerations for contactless power transfer quadrature pick-ups," *IEEE Trans. Ind. Electron.*, vol. 60, no. 1, pp. 400–409, Aug. 2011.

[3] S. Mohagheghi, B. Parkhideh, and S. Bhattacharya, "Inductive power transfer for electric vehicle: Potential benefits for the distribution grid," in *Proc. IEEE Int. Elect. Veh. Conf.*, 2012, pp. 1–8.

[4] J. Deng, F. Lu, S. Li, T. Nguyen, and C. Mi, "Development of a high efficiency primary side controlled 7kW wireless power charger," in *Proc. IEEE Int. Elect. Veh. Conf.*, 2014, pp. 1–6.

[5] D. Chen, L. Wang, C. Liao, and Y. Guo, "The power loss analysis for resonant wireless power transfer," in *Proc. IEEE Transport. Electr. Asia-Pacific Conf.*, 2014, pp. 1–4.

[6] J. Dai and D. Ludois, "A survey of wireless power transfer and a critical comparison of inductive and capacitive coupling for small gap applications," *IEEE Trans. Power Electron.*, vol. 30, no. 11, pp. 6017–6029, Mar. 2015.

[7] F. Lu, H. Zhang, H. Hofmann, and C. Mi, "A double-sided *LCLC*-compensated capacitive power transfer system for electric vehicle charging," *IEEE Trans. Power Electron.*, vol. 30, no. 11, pp. 6011–6014, Jun. 2015.

[8] C. Liu, A. P. Hu, G. A. Covic, and N. K. C. Nair, "Comparative study of CCPT system with two different inductor tuning positions," *IEEE Trans. Power Electron.*, vol. 27, no. 1, pp. 294–306, Jun. 2011.

[9] M. Kline, I. Izyumin, B. Boser, and S. Sanders, "Capacitive power transfer for contactless charging," in *Proc. IEEE Appl. Power Electr. Conf.*, 2011, pp. 1398–1404.

[10] S. Li, W. Li, J. Deng, T. D. Nguyen, and C. C. Mi, "A double-sided LCC compensation network and its tuning method for wireless power transfer," *IEEE Trans. Veh. Technol.*, vol. 64, no. 6, pp. 2261–2273, Aug. 2014.

[11] D. Shmilovitz, A. Abramovitz, and I. Reichman, "Quasi-resonant LED driver with capacitive isolation and high PF," *IEEE J. Emerg. Sel. Topics Power Electron.*, vol. 3, no. 3, pp. 633–641, Apr. 2015.

[12] A. P. Hu, C. Liu, and H. Li, "A novel contactless battery charging system for soccer playing robot," in *Proc. IEEE Int. Conf. Mechantronics Mach. Vis. Practice*, 2008, pp. 646–650.

[13] D. C. Ludois, M. J. Erickson, and J. K. Reed, "Aerodynamic fluid bearings for translational and rotating capacitors in noncontact capacitive power transfer systems," *IEEE Trans. Ind. Appl.*, vol. 50, no. 2, pp. 1025–1033, Jul. 2013.

[14] J. Dai and D. C. Ludios, "Single active switch power electronics for kilowatt scale capacitive power transfer," *IEEE J. Emerg. Sel. Power Electron.*, vol. 3, no. 1, pp. 315–323, Jul. 2014.

[15] L. Huang, A. P. Hu, A. Swwain, and X. Dai, "Comparison of two high frequency converters for capacitive power transfer," in *Proc. IEEE Energy Convers. Congr. Expo.*, 2014, pp. 5437–5443.

[16] B. H. Choi, D. T. Dguyen, S. J. Yoo, J. H. Kim, and C. T. Rim, "A novel source-side monitored capacitive power transfer system for contactless mobile charger using class-E converter," in *Proc. IEEE Veh. Technol. Conf.*, 2014, pp. 1–5.

[17] S. Pasko, M. Kazimierczuk, and B. Grzesik, "Self-capacitance of coupled toroidal inductors for EMI filters," *IEEE Trans. Electromagn. Compat.*, vol. 57, no. 2, pp. 216–223, Jan. 2015.

[18] P. Srimuang, N. Puangngernmak, and S. Chalermwisutkul, "13.56 MHz class E power amplifier with 94.6% efficiency and 31 watts output power for RF heating applications," in *Proc. IEEE Int. Conf. Elect. Eng./Electron., Comput., Telecommun. Inform. Technol.*, 2014, pp. 1–5.

[19] S. Goma. (2012, Nov.). Capacitive coupling powers transmission module. [Online]. Available: http://www.mutata.com/~/media/webrenewal/about/newsroom/tech/power/wptm/ta1291.ashx

[20] T. Komaru and H. Akita, "Positional characteristics of capacitive power transfer as a resonance coupling system," in *Proc. IEEE Wireless Power Transfer Conf.*, 2013, pp. 218–221.

[21] C. Liu, A. P. Hu, and M. Budhia, "A generalized coupling model for capacitive power transfer system," in *Proc. IEEE Ind. Electron. Conf.*, 2010, pp. 274–279.

[22] H. Nishiyama and M. Nakamura, "Form and capacitance of parallel plate capacitor," *IEEE Trans. Compon. Packag. Manuf. Technol. A*, vol. 17, no. 3, pp. 477–484, Sep. 1994.

[23] *IEEE Standard for Safety Levels with Respect to Human Exposure to Radio Frequency Electromagnetic Fields, 3kHz to 300 GHz*, IEEE Standard C95.1, 2005.

[24] F. Lu, H. Hofmann, J. Deng, and C. Mi, "Output power and efficiency sensitivity to circuit parameter variations in double-sided LCC-compensated wireless power transfer system," in *Proc. IEEE Appl. Power Electr. Conf.*, 2015, pp. 597–601.

[25] F. Lu, H. Zhang, H. Hofmann, and C. Mi, "A high efficiency 3.3 kW loosely-coupled wireless power transfer system without magnetic material," in *Proc. IEEE Energy Convers. Congr. Expo.*, 2015, pp. 1–5.

Hua Zhang (S'14) received the B.S. and M.S. degrees in electrical engineering from Northwestern Polytechnical University, Xi'an, China, in 2011 and 2014, respectively, where she is currently working toward the Ph.D. degree in electrical engineering.

From September 2014 to August 2015, she was a joint Ph.D. student founded by the China Scholarship Council with the University of Michigan, Dearborn, MI, USA. From September 2015, she started to work in San Diego State University. Her research interest includes the coupler design of high-power IPT and CPT system.

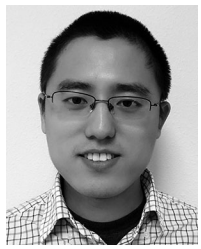

Fei Lu (S'12) received the B.S. and M.S. degrees in electrical engineering from the Harbin Institute of Technology, Harbin, China, in 2010 and 2012, respectively. He is currently working toward the Ph.D. degree in electrical engineering from the University of Michigan, Ann Arbor, MI, USA.

His research topic focuses on wireless power transfer for the application of electric vehicle charging. He is working on the high power and high efficiency capacitive power transfer through an air-gap distance up to 100's of millimeters. He is also working on the application of wide band-gap devices on the WPT system to increase the system frequency.

Heath Hofmann (M'89–SM'15) received the B.S. degree in electrical engineering from the University of Texas at Austin, Austin, TX, USA, in 1992, and the M.S. and Ph.D. degrees in electrical engineering and computer science from the University of California, Berkeley, CA, USA, in 1997 and 1998, respectively.

He is currently an Associate Professor with the University of Michigan, Ann Arbor, MI, USA. His research interests include the design, analysis, and control of electromechanical systems, and power electronics.

Weiguo Liu (SM'07) received the B.S. degree in electrical machines engineering from the Huazhong University of Science and Technology, Wuhan, China, in 1982, and the M.S. degree in electrical engineering, and the Ph.D. degree in control theory and control engineering from Northwestern Polytechnical University, Xi'an, China, in 1988 and 1999, respectively.

He is currently a Professor in the Department of Electrical Engineering, Northwestern Polytechnical University, and a Guest Professor of University of Federal Defense, Munich, Germany. He is the Director of the Institute of Rare Earth Permanent Magnet Electrical Machines and Control Technology, Northwestern Polytechnical University. He was the Chairman of Organizing Committee of the 32nd Chinese Control Conference, July 2013, Xi'an. His research interests include brushless dc Machines, PM synchronous machines, dc machines, and induction machines.

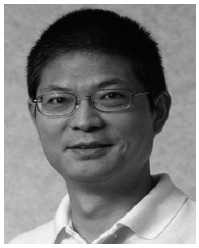

Chunting Chris Mi (S'00–A'01–M'01–SM'03–F'12) received the B.S.E.E. and M.S.E.E. degrees in electrical engineering from Northwestern Polytechnical University, Xi'an, China, and the Ph.D. degree in electrical engineering from the University of Toronto, Toronto, ON, Canada.

He is currently a Professor and the Chair of electrical and computer engineering, and the Director of the Department of Energy-Funded Graduate Automotive Technology Education Center for Electric Drive Transportation, San Diego State University (SDSU), San Diego, CA, USA. Prior to joining SDSU, he was with with University of Michigan, Dearborn, MI, USA, from 2001 to 2015. He was the President and the Chief Technical Officer of 1Power Solutions, Inc., from 2008 to 2011. He is the Co-Founder of Gannon Motors and Controls LLC and Mia Motors, Inc. His research interests include electric drives, power electronics, electric machines, renewable-energy systems, and electrical and hybrid vehicles. He has conducted extensive research and has published more than 100 journal papers. He has taught tutorials and seminars on the subject of HEVs/PHEVs for the Society of Automotive Engineers, the IEEE, workshops sponsored by the National Science Foundation, and the National Society of Professional Engineers. He has delivered courses to major automotive OEMs and suppliers, including GM, Ford, Chrysler, Honda, Hyundai, Tyco Electronics, A&D Technology, Johnson Controls, Quantum Technology, Delphi, and the European Ph.D. School. He has offered tutorials in many countries, including the U.S., China, Korea, Singapore, Italy, France, and Mexico. He has published more than 100 articles and delivered 30 invited talks and keynote speeches. He has also served as a panelist in major IEEE and SAE conferences.

Dr. Mi received the Distinguished Teaching Award and Distinguished Research Award of the University of Michigan. He also received 2007 IEEE Region 4 Outstanding Engineer Award, IEEE Southeastern Michigan Section Outstanding Professional Award, and the SAE Environmental Excellence in Transportation.